nature catalysis

Article

https://doi.org/10.1038/s41929-023-00927-2

Elemental zoning enhances mass transport in zeolite catalysts for methanol to hydrocarbons

Received: 2 February 2021

Accepted: 6 February 2023

Published online: 16 March 2023

Check for updates

Thuy T. Le[1,5], Wei Qin[1,5], Ankur Agarwal[1], Nikolaos Nikolopoulos[2], Donglong Fu[2], Matthew D. Patton[1], Conan Weiland[3], Simon R. Bare[4], Jeremy C. Palmer[1], Bert M. Weckhuysen[2] ✉ & Jeffrey D. Rimer[1] ✉

Mass transport limitations in zeolite catalysts pose major hurdles for their optimal performance in diverse chemical reactions. Most approaches to reduce these restrictions focus on the synthesis of either hierarchical or nanosized zeolites. Here we demonstrate that the existence of a siliceous, catalytically inactive exterior rim on ZSM-5 particles dramatically reduces the diffusion limitations, which leads to an enhanced catalyst lifetime for the methanol-to-hydrocarbon reaction. Our findings reveal that binary inorganic and organic structure-directing agents enable a one-pot synthesis of Si-zoned ZSM-5 catalysts with diffusion properties that are characteristic of particles with a much smaller size. Operando ultraviolet–visible light diffuse reflectance spectroscopy reveals a marked reduction in external coking among Si-zoned samples. Molecular dynamics simulations to assess the diffusion of methanol and benzene in siliceous pores and in those with Brønsted acids reveal substantially reduced transport limitations in zoned regions, consistent with the improved catalyst activity of Si-zoned zeolites relative to that of ZSM-5 with a homogeneous acid-site distribution.

A common objective in zeolite catalyst optimization is the reduction of diffusion limitations through a range of (post)synthesis approaches[1–8], which include the preparation of pillared[2,9] or finned[10] zeolite catalysts. Relatively few studies[11–14] considered the potential impact of spatial gradients in zeolite composition (for example, the Si/Al ratio) on mass transport properties and their concomitant effects on catalyst performance. The spatial distribution of aluminium in zeolites is oftentimes considered to be homogeneous; however, mesoscopic[14–18] gradients can exist in the form of aluminium zoning, most frequently observed in zeolite ZSM-5, in which aluminium is disproportionately concentrated in the exterior rim of the zeolite particle[19–23]. An alternative and less commonly reported configuration is silicon zoning, in which the exterior rim of the crystals is enriched in silicon[20]. Given that the shape selectivity of zeolites is derived from Brønsted acid sites located within the confined pore network[16], it was demonstrated that postsynthesis modification of zeolite ZSM-5 catalysts with a siliceous exterior (or passivated surface) eliminates non-selective reactions on external surfaces[17,18,24,25] or generates a hydrophobic exterior that is beneficial for select applications[26,27]. Methods to either passivate or remove external Brønsted acid sites can have deleterious side effects, such as a sacrificed catalyst activity via pore blockage[28,29] or the generation of defects as a result of zeolite dealumination[30,31]. Therefore, it is desirable to identify facile and more efficient methods to produce Si-zoned zeolite ZSM-5 catalysts.

[1]Department of Chemical and Biomolecular Engineering, University of Houston, Houston, TX, USA. [2]Inorganic Chemistry and Catalysis Group, Institute for Sustainable and Circular Chemistry and Debye Institute for Nanomaterials Science, Faculty of Science, Utrecht University, Utrecht, the Netherlands. [3]Materials Measurement Science Division, Material Measurement Laboratory, National Institute of Standards and Technology, Gaithersburg, MD, USA. [4]SLAC National Accelerator Laboratory, Menlo Park, CA, USA. [5]These authors contributed equally: Thuy T. Le, Wei Qin. ✉e-mail: b.m.weckhuysen@uu.nl; jrimer@central.uh.edu

The majority of studies that examined the spatial distribution of acid sites in zeolites focused on a microscopic level to determine the catalytic consequences of isolated or paired Al sites in zeolite frameworks[32–34]. Here we focus on the effects of mesoscopic elemental zoning, which are largely unexplored. We report methods to prepare both Si- and Al-zoned zeolite ZSM-5 via one-pot syntheses based on the judicious selection of organic and/or inorganic structure-directing agents (SDAs). Structure–performance relationships in methanol-to-hydrocarbon (MTH) reactions are established for zoned catalysts in comparison with zeolite ZSM-5 with a homogeneous Al distribution using an experimentally derived descriptor that takes into account three critical physicochemical properties: mass transport, acid site concentration, and surface area. Our combined experimental and computational findings reveal that the introduction of a siliceous outer layer on Si-zoned zeolite ZSM-5 leads to unexpected and dramatic improvements in the mass transport properties with a concomitant enhancement in catalyst performance.

Results

Synthesis of zoned zeolite ZSM-5 crystals

We adapted two reported protocols for synthesizing zeolite ZSM-5 in growth mixtures comprised almost solely of an organic (that is, tetrapropylammonium, TPA^+) (ref. [35]) or exclusively with an inorganic (Na^+) (ref. [36]) SDA. The conditions of these two syntheses also differ with respect to temperature (100 versus 190 °C, respectively) and silicon source (tetraethyl orthosilicate versus colloidal silica, respectively). Elemental analysis using a combination of energy dispersive X-ray spectroscopy and X-ray photoelectron spectroscopy (XPS) were performed to assess the Si/Al ratio of the entire crystal (bulk) and the outermost layer (surface) to determine if there was Si or Al zoning (Fig. 1a). Both synthesis protocols yielded ZSM-5 zeolites with a homogeneous distribution of Al, as indicated by their equivalent bulk and surface Si/Al ratios. Interestingly, modifications of the synthesis composition that involved mixtures of both organic and inorganic SDAs resulted in the formation of zoned ZSM-5 materials in which the degree of zoning increased monotonically as the ratio of SDAs approached a 50:50 organic/inorganic combination (Fig. 1b,c). For syntheses in organic-rich media at a lower temperature, the combination of TPA^+ and Na^+ resulted in Al-zoned ZSM-5 (Fig. 1b), whereas for inorganic-rich media at a higher temperature the combination yielded Si-zoned ZSM-5 (Fig. 1c). For comparison, we tested the effect of partially replacing Na^+ with K^+, which was shown to enhance the rate of ZSM-5 crystallization and alter Al incorporation[37,38]. Our findings revealed similar trends in the Si/Al ratio for both alkali metals.

Here we focus on six samples using a naming convention for zeolite ZSM-5 materials with a homogeneous Al distribution (H*x*-*y*), Al zoning (A-*y*) and Si zoning (S*x*-*y*), where *x* refers to the sample number and *y* refers to the effective crystal size (in micrometres) estimated from diffusion measurements. Powder X-ray diffraction patterns of all the samples (Supplementary Figs. 1–3) confirmed the MFI framework structure of ZSM-5 without evidence of any impurities or residual amorphous material. Scanning electron microscopy (SEM) images of zeolite samples (Fig. 2) revealed the distribution of crystal size and morphology. The Al-zoned sample (A-4) has the smallest crystal size (Fig. 2a, ~1 µm in diameter). Homogeneous samples (H1-3 and H2-6) exhibited a similar size by SEM, but disparate morphology depending on synthesis conditions (Fig. 2b,c). Si-zoned samples (S1-1, S2-1 and S3-2) exhibited a similar morphology with differences in crystal size that spanned from 3 to 12 µm (Fig. 2d–f, respectively).

Few studies in literature reported the direct synthesis of Si-zoned ZSM-5 (refs. [39–41]), and even fewer explored the mechanism of zoning[42–44]. Although the exact mechanism of formation is unknown, we posit that the origin of Si zoning is related to the relative rates of Si and Al depletion from growth media at various stages of crystallization compared with that of ZSM-5 samples with a homogeneous

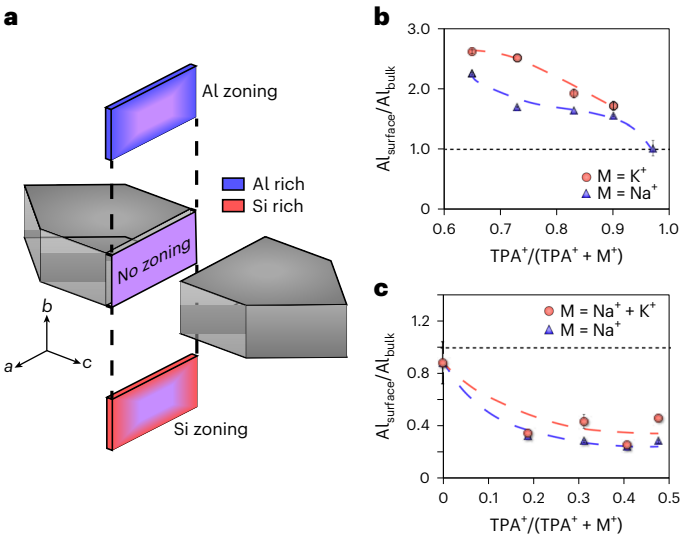

Fig. 1 | Synthesis of zeolite ZSM-5 with elemental zoning. a, Idealized depiction of Al and Si zoning in zeolite ZSM-5. **b**, Ratio of surface-to-bulk aluminium, $Al_{surface}/Al_{bulk}$, for Al-zoned zeolites after three days of hydrothermal treatment at 100 °C as a function of the organic SDA fraction (TPA^+) in the growth mixture. Samples prepared with M = Na^+ and M = K^+ are listed in Supplementary Table 1. Symbols are the average of two measurements and error bars span two standard deviations for selected samples. **c**, Values of $Al_{surface}/Al_{bulk}$ for Si-zoned zeolites after one day of hydrothermal treatment at 190 °C as a function of the organic SDA fraction (TPA^+) in the growth mixture. The sample with $Al_{surface}/Al_{bulk} \approx 1$ is from an organic-free synthesis (sample ZH2 in Supplementary Table 2). The total alkali concentration was fixed by the addition of NaCl or partial addition of KCl, as listed in Supplementary Tables 2 and 3. Symbols are the average of two measurements and error bars span two standard deviations for selected samples. Dotted black lines indicate homogeneous zeolites with $Al_{surface}/Al_{bulk} = 1$, and dashed blue and red lines are interpolated to guide the eye.

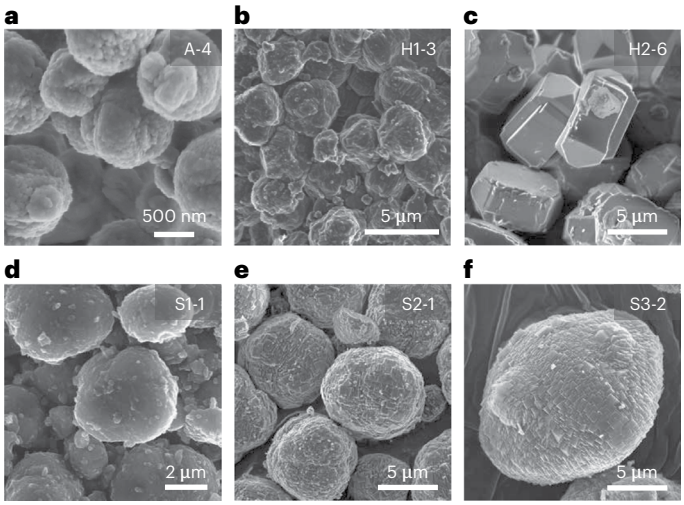

Fig. 2 | Crystal habit of the zeolite ZSM-5 samples under study. a–f, SEM images of Al-zoned sample A-4 (**a**), homogeneous samples H1-3 (**b**) and H2-6 (**c**), and Si-zoned samples S1-1 (**d**), S2-1 (**e**) and S3-2 (**f**). All the syntheses were performed at 190 °C, with the exception of sample A-4 at 100 °C. Details of the synthesis conditions are provided in Supplementary Table 4 and their physicochemical properties are listed in Table 1.

Al distribution, consistent with time-resolved measurements of the supernatant Si and Al composition over a 24 hour period of hydrothermal treatment at 190 °C (Supplementary Figs. 4–6). Depth profiling

https://doi.org/10.1038/s41929-023-00927-2

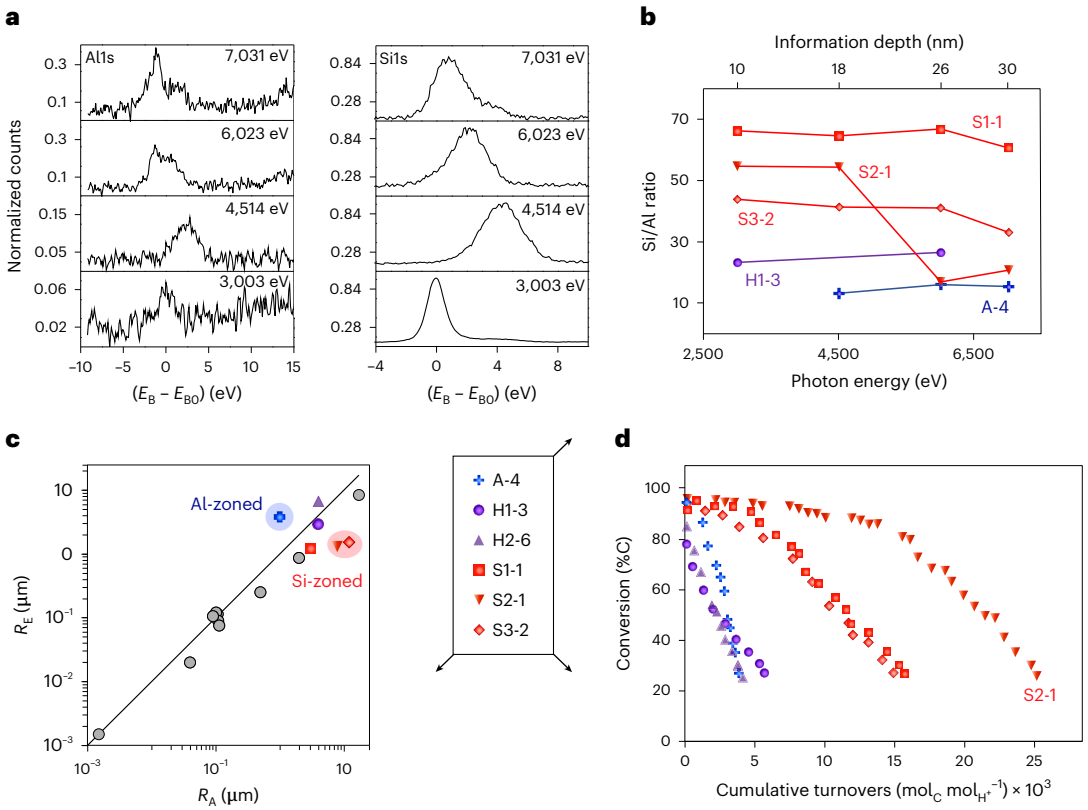

Fig. 3 | Characterization of zeolite ZSM-5 zoning and catalyst performance. **a**, VKE–XPS spectra collected at four different photon energies for sample S2-1. The binding energy (E_B) is plotted relative to the binding energy of spectra collected at a photon energy of 3,003 eV (E_{BO} = 1,839.2 eV for Si 1*s* and 1,559.2 eV for Al 1*s*). See Supplementary Figs. 12 and 13 for the spectra of other samples. **b**, Si/Al ratios from XPS depth analysis of five samples (excluding H2-6) as a function of photon energy and the corresponding information depth. Purple, homogeneous; red, Si-zoned; blue Al-zoned. **c**, Parity plot in log scale of R_E (calculated from sorption measurements) against R_A measured from SEM images of H-ZSM-5 samples (average of more than 20 crystals). The solid line indicates equivalent sizes ($R_E = R_A$) and the grey circles are data collected from the literature[46,49]. **d**, Conversion of methanol and dimethyl ether (DME) as a function of cumulative turnovers for the Al-zoned sample (A-4), homogeneous samples (H1-3 and H2-6) and Si-zoned samples (S1-1, S2-1 and S3-2). All the reactions were performed at 350 °C using a space velocity of 0.18–0.30 $mol_{MeOH}\ mol_{H^+}^{-1}\ s^{-1}$.

Table 1 | Physicochemical properties of the zeolite ZSM-5 samples selected for catalyst testing

Catalyst sample	R_A (μm)[a]	R_E (μm)	S/B	BET S_A ($m^2 g^{-1}$)	$V_{micropore}$ ($cm^3 g^{-1}$)	Si/Al ratio[b]	C_{acid} (μmol g^{-1})[c]	Acid type (%)[d]		EFAl (%)[e]
								B	L	
A-4	1.1±0.2	3.8	1.7	409	0.08	28	531	NA[f]	NA[f]	12
H1-3	4.0±0.3	2.9	1.04	405	0.12	28	673	82	18	6
H2-6	4.0±0.5	6.4	0.88	370	0.12	21	941	88	12	7
S1-1	3.0±0.9	1.2	0.27	431	0.12	29	730	85	15	7
S2-1	8.0±0.7	1.3	0.32	403	0.12	37	578	83	17	3
S3-2	12±1	1.6	0.42	416	0.12	29	773	85	15	6

[a]Values are the average and standard deviation measured for at least 20 crystals in SEM images; the crystal size of H2-6 corresponds to the *b* direction. [b]Measured by inductively coupled plasma atomic emission spectroscopy. [c]Measured by NH_3 temperature programmed desorption (Supplementary Fig. 10). [d]Measured by pyridine FTIR spectroscopy. [e]Measured by ^{27}Al magic angle spinning NMR (Supplementary Fig. 11). [f]Not quantifiable due to negligible adsorption of pyridine. A, Al-zoned; H, homogeneous; S, Si-zoned; S/B, surface-to-bulk Al ratio; B, Brønsted acid sites; L, Lewis acid sites; EFAl, higher extra-framework Al.

of the Si/Al ratio was conducted using variable kinetic energy X-ray photoelectron spectroscopy (VKE–XPS). In these experiments, the integrated areas of the Al 1*s* and Si 1*s* peaks (Fig. 3a) were used to calculate the Si/Al ratio of each sample as a function of the photon energy and information depth, taken as three times the inelastic mean free path (Fig. 3b). VKE–XPS confirmed that all the Si-zoned samples had higher surface Si/Al ratios than those of the homogeneous samples. There is an obvious decrease in the Si/Al ratio with increased information depth for the three Si-zoned samples, as expected for Si-zoned samples with a Si-rich exterior and an interior with a higher Al content. The Si-zoned sample S2-1 was distinct from others in that it exhibited a sharper decrease in the Si/Al ratio, indicative of a thinner siliceous outer rim in comparison to those of samples S1-1 and S3-2.

Comparison of catalyst performance

As-synthesized ZSM-5 samples were ion exchanged with NH_4^+ and calcined to produce Brønsted acids (H-form catalysts). The physicochemical properties of all the corresponding H-ZSM-5 catalysts

https://doi.org/10.1038/s41929-023-00927-2

used in the MTH reactions are provided in Table 1. Textural analysis (Supplementary Fig. 7) revealed a lower micropore volume for Al-zoned sample A-4 and the presence of small internal voids in Si-zoned samples, which was confirmed by focused ion beam cross-sectional images (Supplementary Fig. 7c,d). Solid-state ^{27}Al magic angle spinning nuclear magnetic resonance (NMR) spectroscopy also revealed that sample A-4 had a higher extra-framework Al content (that is, approximately twice that of the other samples). Elemental analysis by inductively coupled plasma atomic emission spectroscopy revealed a relatively narrow range of Al content among all the samples (Si/Al = 21 to 37). The apparent crystal size, R_A, of each sample estimated from the SEM images is reported in Table 1; however, we also determined an effective size, R_E, using a reported protocol[45,46] in which the effective diffusion timescale (R_E^2/D), where D is an effective diffusion coefficient measure for silicalite-1 at 110 °C from the literature, was measured from time-resolved 2,3-dimethylbutane sorption experiments (Supplementary Fig. 8)[47]. Early uptake times were fitted with a separate model reported by Gao et al.[48] to extract the surface permeability α (Supplementary Fig. 9 and Extended Data Fig. 1). Detailed descriptions of these measurements and data fitting are provided in Methods.

Si-zoned samples exhibited a higher surface permeability ($\alpha \approx 0.12$ μm s^{-1}) than homogeneous ($\alpha = 0.02$–0.08 μm s^{-1}) and Al-zoned ($\alpha \approx 0.03$ μm s^{-1}) samples (Extended Data Fig. 1), which is similar to the trends observed by Gao et al.[48] for α as a function of zeolite Al content. Interestingly, there were noticeable differences between the sizes estimated from microscopy and those from sorption measurements. The parity plot in Fig. 3c reveals that the Si-zoned samples had effective sizes that were less than their apparent sizes (that is, as much as eightfold less), whereas the Al-zoned sample had a larger R_E (about fourfold larger), which seems to indicate the presence of defects that result in mass transport restrictions, which is consistent with its notably lower microporous volume. Given that the majority of naturally zoned ZSM-5 reported in the literature are Al-zoned materials, we included sample A-4 to highlight the potential defects present in Al-zoned zeolites and their impact on catalyst performance. For comparison, we also plotted values reported by Bhan and coworkers[46,49] for ZSM-5 catalysts spanning a broad range of sizes ($R_A = 2$ nm to 17 μm) in which their dimensions R_A and R_E were either nearly equivalent or had a smaller R_E (within a twofold difference). Homogeneous sample H1-3 falls close to the parity line, whereas homogeneous H2-6 and Al-zoned A-4 are the only samples to have an R_E larger than their R_A.

The catalyst performance in the MTH reaction (Fig. 3d) was assessed at a subcomplete conversion (<96%) using a similar molar contact time for all the samples. As a proxy for time on stream (TOS), we used the turnover number (TON), as described in Methods (equation (3)). Surprisingly, all the Si-zoned samples markedly outperformed the homogeneous samples with lifetimes extended by as much as fourfold compared with that of H1-3. The activity of the Al-zoned sample was slightly prolonged in the early TOS but exhibited the fastest rate of deactivation among the samples tested in this study (that is, the slope of the linear regions in Fig. 3d). There are distinct differences between the two homogeneous samples, with H2-6 being about twofold less stable than H1-3. One factor that can explain the poor performances of samples H2-6 and A-4 is their large R_E relative to R_A, which is indicative of diffusion limitations imposed by putative defects that compromise catalyst lifetimes (vide infra). Another interesting observation is the exceptionally long lifetime of S2-1 among the three Si-zoned samples despite similarities in R_E values. Although the S2-1 sample has a slightly higher Si/Al in the core compared with those of the other two samples, according to a study on effect of Al content by Bhan and coworkers, it is unlikely to contribute to a large difference in performance[49]. One factor that may contribute to its superior performance is the relatively thin region of silicon zoning, as indicated by the VKE–XPS data (Fig. 3b).

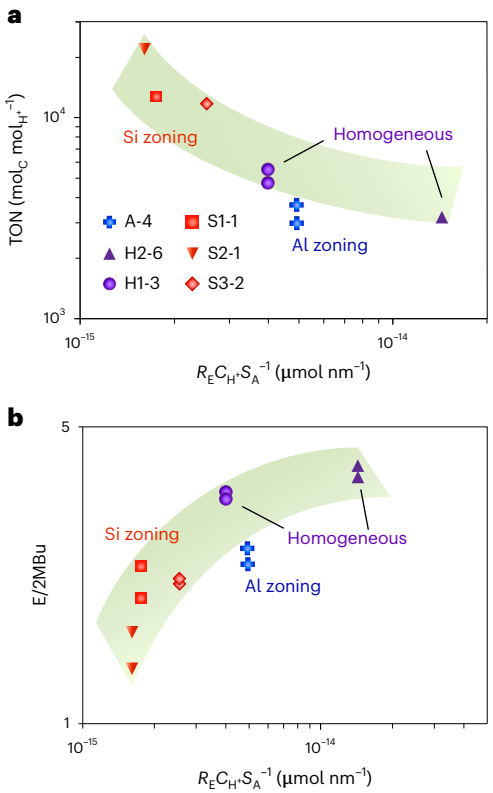

Fig. 4 | Descriptor-based comparison of zeolite ZSM-5 catalyst performance. **a**, The TON for H-ZSM-5 catalysts calculated from conversion versus TOS data (Extended Data Fig. 2a) as a function of the descriptor $R_E C_{H^+} S_A^{-1}$. Data include repeat measurements of catalysts prepared from different synthesis batches. The TON values were calculated until the times at each catalyst reached 20% conversion (details in Methods). **b**, Corresponding ratios of ethene to 2MBu (E/2MBu) for each sample. The zoned trend in Fig. 4b is qualitatively consistent with that reported in the literature (Supplementary Fig. 12). The shaded green regions mark approximate trends. Refer to Supplementary Table 5 for the actual values of the descriptor, TON and E/2MBu. Product selectivity profiles for each catalyst are provided in Extended Data Fig. 2b.

Owing to the complexity of the MTH reaction and the effects of various physicochemical properties on the catalytic performance[50–52], we introduced a structure-performance descriptor, $R_E C_{H^+} S_A^{-1}$, which is inspired by the approaches reported by the groups of Bhan[49,53] and Gascon[54] with a slight modification to facilitate side-by-side comparisons of the catalysts. The physical meaning of the descriptor is the total number of acid sites that a molecule encounters over the net diffusion path length. The descriptor accounts for mass transport (R_E, or diffusion path length) and total acid sites, analogous to Bhan's approach in which the parameter C_{H^+} used here is the total concentration of Brønsted acid sites measured from combined NH_3 temperature programmed desorption (TPD) and pyridine Fourier transform infrared (FTIR) spectroscopy, noting that Brønsted acids are the primary active sites for MTH. We also account for the Brunauer–Emmett–Teller surface area (BET S_A) used by Gascon, which yields a descriptor with units of moles of Brønsted acids per unit length, in close agreement with the descriptor that was mathematically derived by Bhan and coworkers (that is, number of Al sites per unit length)[49]. We assessed the performance of each catalyst and found that trends in TON were absent when comparisons were made on the basis of individual properties (for example, R_E, $C_{H^+}$and so on); however, the clear trend that emerges when data are plotted in the log–log scale as a function of the descriptor (Fig. 4a) is qualitatively consistent with a trend reported for SAPO-34

https://doi.org/10.1038/s41929-023-00927-2

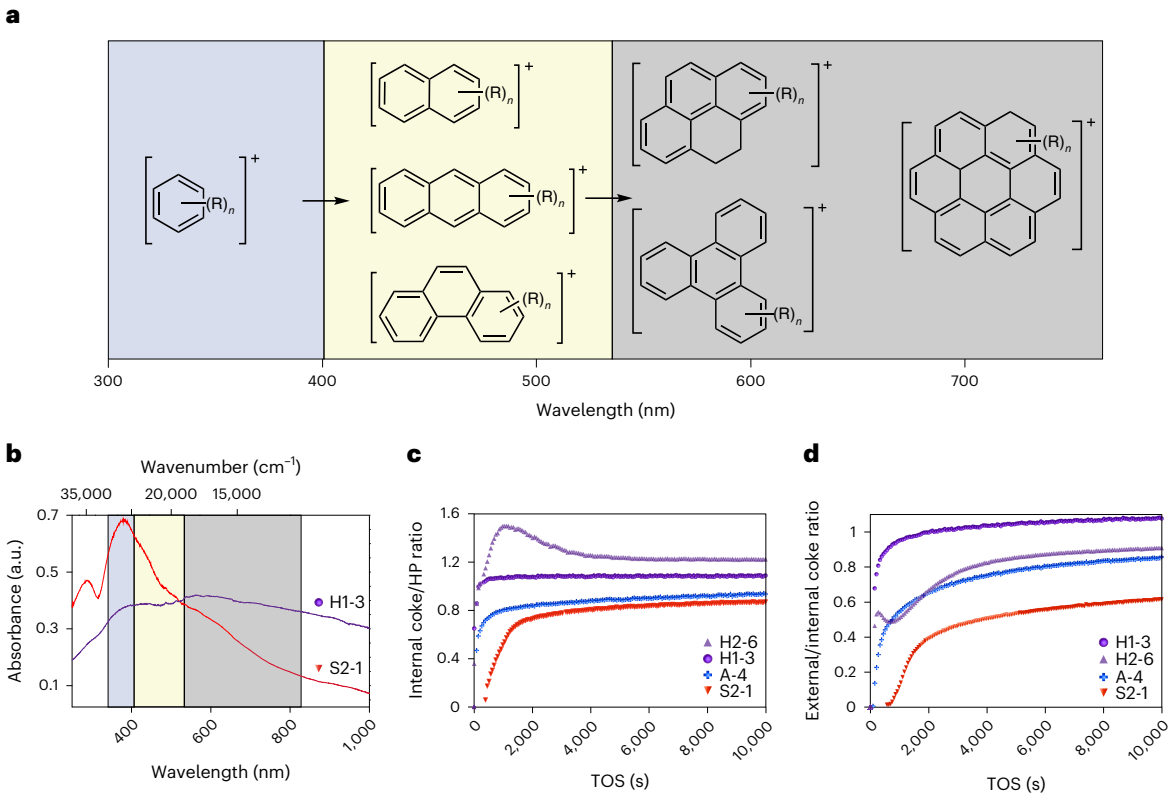

Fig. 5 | Tracking product evolution by operando UV–vis DR spectroscopy. **a**, UV–vis absorption bands corresponding to HP species (blue), internal coke (yellow) and external coke (grey) (precursor) molecules during the MTH reaction based on previous assignments[55]. **b**, Operando UV–vis DR spectra of selected catalysts after 9,990 s of MTH reaction at 350 °C (see Supplementary Figs. 15 and 16 for the full set of samples). **c**, Temporal changes of the intensity ratio of internal coke (precursor) species (416–425 nm) to HP species (350–375 nm) during the reaction as a function of TOS. **d**, The corresponding changes of the intensity ratio of external coke (precursor) species (560–575 nm) to internal coke (precursor) species. The UV–vis absorption band positions selected for each sample are provided in Supplementary Table 6. a.u., arbitrary units.

catalysts in the MTH reaction[53]. The indicator E/2MBu for the dual cycle mechanism, which represents the ratio of ethene to the sum of 2-methylbutane and 2-methylbutene, is plotted in Fig. 4b (log–log scale) as a function of the descriptor and we observe a decrease in the E/2MBu ratio with decreasing values of the descriptor, in accordance with reported trends for ZSM-5 catalysts in MTH reactions (Supplementary Fig. 14), in which the reduction of mass transport limitations and/or average active sites encountered by the reactive species led to a weaker propagation of the aromatic cycle in the hydrocarbon pool (HP) mechanism[49].

The data in Fig. 4 show one of the few examples in which trends in the MTH lifetime and selectivity are directly compared as a function of multiple catalyst properties. Interestingly, we see an inverse relationship in which an increased TON correlates with a reduced E/2MBu ratio, which indicates the olefin-based cycle was promoted at lower values of $R_E C_{H^+} S_A^{-1}$. Previous studies showed how each factor (Al content and effective size) individually impacts the propagation of olefin and aromatic cycles[46,49]. Coupling both factors in a single descriptor yields monotonic trends; however, the Al-zoned sample (A-4) appears to defy the trends, given that its E/2MBu ratio is equivalent to that of Si-zoned sample S1-1 and there is a fourfold difference in TON values. This highlights the capability of a descriptor to identify outliers among catalyst samples, and thus pinpoint the impact of synthesis conditions on catalyst performance. For instance, the homogeneous samples were prepared using growth solutions with predominantly organic (H1-3) or inorganic (H2-6) SDAs, of which the latter generates a less effective catalyst. Alternatively, different performances of the Si-zoned samples with growth mixtures that contained Na^+ and TPA^+ (sample S2-1) and Na^+, K^+ and TPA^+ (samples S2-1 and S3-2) were also observed, which suggests that different cations used in synthesis can also affect catalytic performance. From our VKE–XPS results, we can speculate that the use of Na^+, compared with that of both Na^+ and K^+, extends the region of zoning; however, additional catalytic studies of samples prepared with a range of cation ratios are needed to draw definitive conclusions.

Deactivation mechanism of zeolite ZSM-5 catalysts

To further understand the catalytic behaviours of these samples, operando ultraviolet–visible (UV–vis) diffuse reflectance (DR) spectroscopy was utilized to follow the evolution of reactive intermediates, or HP species, as well as both internal and external coke (precursor) molecules[47,55–57]. The catalysts were tested in a packed-bed reactor configuration comparable to that used for performance testing, with time-resolved UV–vis DR spectra of the catalyst collected during reaction. Here we correlate three regions of the spectra into generic groupings (Fig. 5a) of HP species, internal coke species and external coke species.

Comparison of the UV–vis DR spectra for representative homogeneous (H1-3) and Si-zoned (S2-1) samples (Fig. 5b) reveals a notable reduction in external coke relative to HP species for the zoned catalyst. Using selected peaks in each spectrum (Supplementary Table 6), we report a ratio of internal coke to HP species (Fig. 5c). The Si-zoned catalyst S2-1 has the lowest intensity ratio among all the samples, which is qualitatively consistent with its longer lifetime (Fig. 3d). The presence of a siliceous exterior also suppresses the formation of external coke, illustrated by the lower ratio of external to internal coke species for S2-1

https://doi.org/10.1038/s41929-023-00927-2

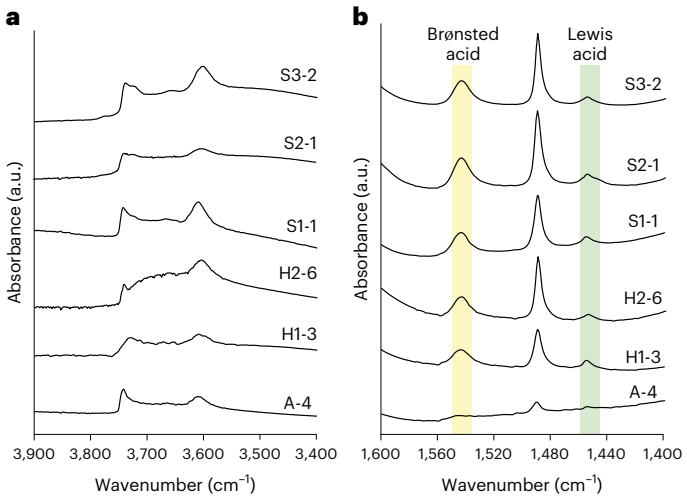

Fig. 6 | FTIR spectroscopic characterization of zeolite ZSM-5 samples. **a**, Spectra in the range 3,900–3,400 cm^{-1} for H-form samples before pyridine adsorption. Bands were assigned according to the literature[60] as external silanol groups (~3,745 cm^{-1}), internal silanol groups (3,720–3,710 cm^{-1}), partially extra-framework Al (~3,665 cm^{-1}), Brønsted acid sites (~3,615 cm^{-1}) and silanol nests (~3,500 cm^{-1}). **b**, Spectra in the range of 1,600–1,400 cm^{-1} after pyridine adsorption. Peaks characteristic of Brønsted acids (maximum around 1,545 cm^{-1}) and Lewis acids (maximum around 1,450 cm^{-1}) are highlighted in yellow and green, respectively.

(Fig. 5d). This suggests that the Si-zoned catalyst exhibits the least degree of external coking compared with that of other samples. A similar suppression of internal (Supplementary Fig. 16a) and external (Supplementary Fig. 16b) coke was observed for the other two Si-zoned samples (S1-1 and S3-2). Notably, sample S2-1 stands out as having the lowest ratios of coke species, which is also reflected in its TON being twofold higher than those of other Si-zoned samples (Supplementary Table 5). The exceptional performance of S2-1 among the Si-zoned samples can be ascribed to its lower overall Brønsted acid concentration (Table 1), which is reflected in its lowest $R_E C_{H^+} S_A^{-1}$ value (Fig. 4), in addition to it having the thinnest Si-rich exterior region of zoning (Fig. 3b).

There are clear differences between both homogeneous samples—the one prepared with Na^+ (H2-6) had a lower TON and larger R_E than the one prepared with TPA^+ (H1-3). The former had the highest ratio of internal coke to HP species (Fig. 5c) with a distinct maximum observed in the early TOS. The preferential deactivation of H2-6 by internal coking can be interpreted as an initial build-up of coke species due to diffusion limitations; and with an extended TOS, a larger fraction of coke precursors reached the external surface, which led to a delayed increase in external coke (Fig. 5d). The disparity in size ($R_E > R_A$) for H2-6 (Fig. 3c) is suggestive of crystalline defects, which is consistent with the textural analysis (Table 1), catalysis results and spectroscopy measurements (vide infra), in which we observed a more prominent broad band in the FTIR spectrum of H2-6 (Fig. 6a) in the region associated with internal silanol groups (~3,650–3,720 cm^{-1}). The presence of internal silanol groups had previously been correlated with deactivation by Beato and coworkers[58], who refer to these sites as internal defects that slow the diffusion of hydrocarbon products and/or stabilize the adsorption of coke precursors. In a separate study, Valtchev and coworkers[59] demonstrated that ZSM-5 catalysts with fewer internal silanol groups are more active and resistant to deactivation. The more active homogeneous sample (H1-3) has fewer internal silanol groups (Fig. 6a) and fewer diffusion limitations ($R_E \approx R_A$; Fig. 3c). Collectively, the set of homogeneous HZSM-5 catalysts provides evidence that an increased number of crystalline defects can shift the predominant mode of deactivation from external coking (H1-3) to internal coking (H2-6).

Operando UV–vis DR spectroscopy data for the Al-zoned sample (A-4) diverges from the above interpretations. This can be explained on the basis of diffusion limitations ($R_E/R_A \approx 4$) that lead to a short lifetime (Fig. 3d) and a TON that is comparable to that of the less active homogeneous sample H2-6 (Supplementary Table 5). Interestingly, the ratio of internal coke to HP species for A-4 is lower than that of both homogeneous samples (Fig. 5c) and its external-to-internal coke ratio is nearly equivalent to that of H2-6 (Fig. 5d). The intermediate levels of internal and external coking for A-4 complicate the assignment of its predominant mode of deactivation. Acid-site titration by pyridine–FTIR spectroscopy yields a low-intensity spectrum in which the relative percentages of Brønsted and Lewis acids cannot be resolved (Fig. 6b)[60]. This suggests pore narrowing and/or pore blockage in the Al-zoned sample, which could be associated with its relatively high percentage of extra-framework Al (Table 1) or may reflect partially coordinated framework Al that was previously reported for Al-zoned ZSM-5[13]. These defective Al sites impose extreme diffusion limitations that promote internal coking and lead to a lower external coking than would be expected on the basis of its high surface Al concentration (Table 1). Similar ratios of internal coke to HP species for Al- and Si-zoned samples observed in Fig. 5c may be attributed to an inaccessible fraction of active sites in sample A-4 as a result of defective Al, which could explain why the poor performance of Al-zoned ZSM-5 deviates from the trends of other catalysts (Fig. 4).

To further assess the impact of zoning on coke formation, we used thermogravimetric analysis to characterize the spent catalysts (Supplementary Table 7). These data reveal a trend of increasing TON with decreasing total coke percentage (Extended Data Fig. 3); however, in cases where there were disparities in this trend, operando UV–vis DR measurements of coke (precursor) species (Fig. 5) were capable of providing valuable insights into the nature of the catalyst deactivation. For example, samples H1-3 and S3-2 had comparable coke percentages, but nearly a twofold higher TON for S3-2 (Fig. 4a), which is attributed to the lower external-to-internal coke ratio of the Si-zoned catalyst (Supplementary Fig. 16b) compared with that of the homogenous catalyst (Fig. 5d).

Computational Validation of Enhanced Diffusion

To demonstrate the enhanced mass transport of both reactants and products in Si-zoned materials, we performed umbrella sampling molecular dynamics (USMD) simulations to characterize the free energy barriers to diffusion through the interior of an MFI's straight channel. For these calculations, we considered three different cases: MFI substituted with aluminium sites (Si/Al = 23) occupied by a methoxy group (MFI-CH_3) or Brønsted acid (MFI-H), and purely siliceous MFI (silicalite-1). As suggested by recent first-principles calculations[61], favourable Al substitutions were created by siting Al at the tetrahedral T8 site in the straight channel and adding a methoxy group or hydrogen to the neighbouring oxygen O17 site (MFI-CH_3 and MFI-H, respectively; Supplementary Fig. 17). In each material, free energy profiles were calculated at 350 °C for the guest species methanol (reactant) and benzene (a prototypical, bulky aromatic product) along the order parameter q (described in Methods) that characterizes the position of each guest species along the major axis of the straight channel.

The free energy profiles for methanol in the interior of MFI's straight channel exhibit periodicity commensurate with the unit cell (Fig. 7a). They exhibited global minima at $q \approx 0$ and 1 nm at the intersections of the MFI straight and sinusoidal channels (state I in Fig. 7a) and high free energy regions at intermediate values as methanol passed through the ten-member ring straight channel. In the low loading limit, the effective free energy barriers to diffusion were several times larger than the thermal energy $k_B T \approx 0.0537$ eV at $T = 350$ °C (k_B is the Boltzmann constant). As a result, molecular transport is characterized

https://doi.org/10.1038/s41929-023-00927-2

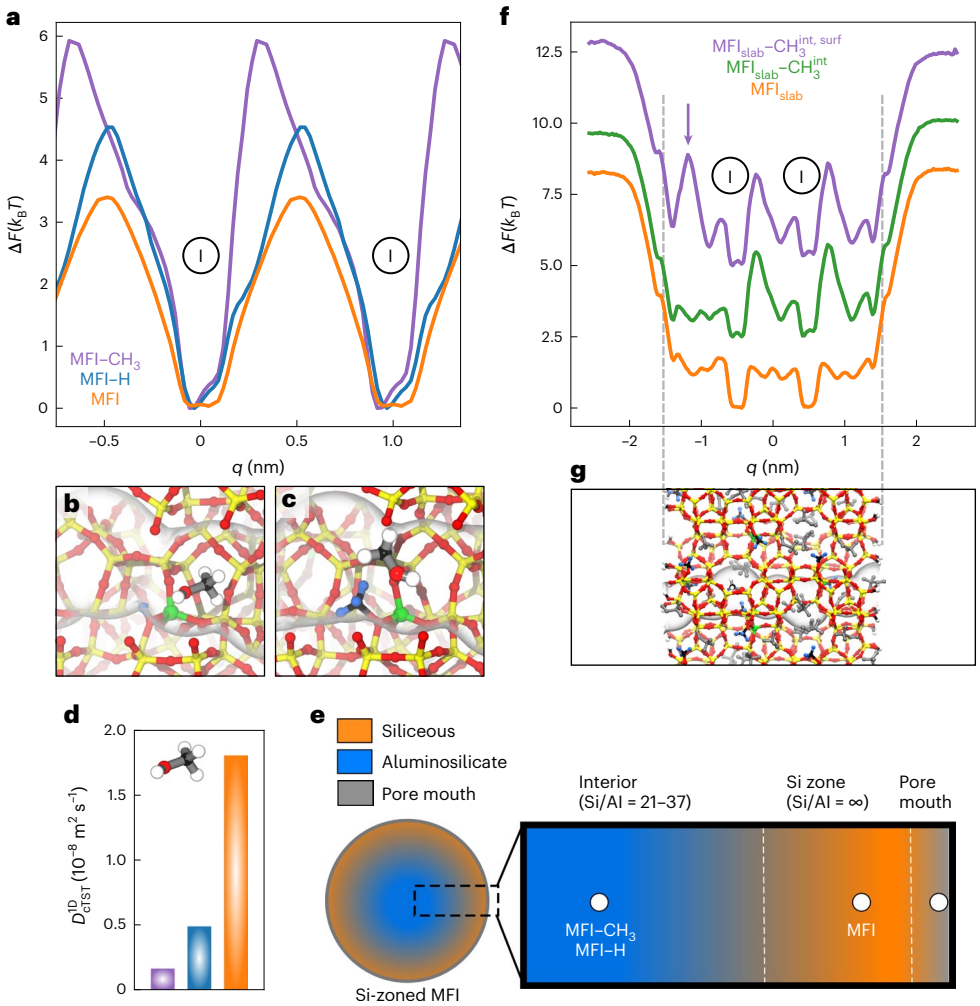

Fig. 7 | Free energy barriers for methanol diffusion in MFI. a, Free energy profile at 350 °C (potential of mean force, in units of the thermal energy; $k_B \approx 0.0537$ eV at $T = 350$ °C) for internal diffusion in the low loading limit through the straight channel (*b* direction) of MFI with: aluminium sites (Si/Al = 23) occupied by methoxy groups (MFI–CH_3) and Brønsted acids (MFI–H) and a purely siliceous material (MFI). **b**,**c**, Images of methanol diffusing through a straight channel populated with Brønsted acid (**b**) and methoxy groups (**c**) (see Supplementary Movies 1 and 2). **d**, Diffusivities for methanol in the low loading limit estimated using dynamically corrected TST (cTST). **e**, Schematic showing the acidic interior, Si zone and pore mouth regions of the MFI catalysts. **f**, Free energy profiles for the methanol surface permeation at a high loading (16 methanols per unit cell) across quasi-2D MFI slabs with aluminium sites (Si/Al ≈ 23) occupied by methoxy groups located at both the external surface and internal region ($MFI_{slab}–CH_3^{int,surf}$) or only the internal region ($MFI_{slab}–CH_3^{int}$) and a purely siliceous material (MFI_{slab}). Profiles are shifted by 2.5 k_BT for clarity. The purple arrow denotes the location of the free energy barrier to permeation. **g**, A rendering of a quasi-2D MFI slab model viewed along [100] direction. Vertical dashed lines denote the position of the slab's surfaces.

by activated processes that involve infrequent hops between adjacent intersection sites[62]. The interactions of methanol with the methoxy groups and Brønsted acid sites within the ten-member ring increase the effective barriers to diffusion in the order MFI–CH_3 > MFI–H > MFI. The methoxy groups, which were expected to be prevalent under the MTH reaction conditions, were bulkier than the Brønsted acid sites and sterically hindered the transport of methanol (Fig. 7b,c). Similar qualitative trends were observed in the free energy profiles for benzene (Extended Data Fig. 4). Whereas the free energy profiles for methanol exhibited a single global maximum, the high free energy region for benzene was populated with local minima. The latter are due to the presence of additional (metastable) sorption sites for benzene in this region and were observed previously in free energy calculations for silicalite-1 (ref. [63]). At high loadings (16 methanols per unit cell) similar to those expected under MTH reaction conditions, the free energy barriers to diffusion for methanol decreased due to the blockage of favourable absorption sites by other molecules, but the presence of methoxy groups still hindered transport (Extended Data Fig. 4). Assuming that transport occurs by a hopping mechanism, the diffusivities for the guest species through the straight channels can be estimated from the free energy profiles using dynamically corrected transition state theory (cTST) (Methods)[62,64]. The diffusivities of guest species were significantly smaller in the Al-substituted materials (by factors of approximately 9 and 5 for methanol and benzene in the low loading limit), which suggests faster mass transport in Si-zoned regions.

The computational results suggest that internal diffusion in the MFI catalyst's Si zone is enhanced relative to its acidic interior due to interactions with methoxy groups and Brønsted acid sites that hinder transport. Although these calculations focus on internal diffusion in the Si-zoned and acidic interior (Fig. 7e), prior studies demonstrate that barriers to surface permeation may also strongly influence molecular transport in nanoporous materials[65–68]. In zeolites, these barriers may arise from a strong surface adsorption or partial pore blocking at the surface, which may be attributed to acid groups or structural defects near the pore mouth (Fig. 7e). Thus, additional free energy calculations were performed to examine the effects of surface

adsorption and partial pore blocking by acid sites on the barriers to permeation across the MFI's (010) face. The permeation barriers were characterized for quasi-two-dimensional (2D) MFI slabs with hydroxyl surface terminations created by cleaving a 3D supercell (Methods). We considered slabs substituted with Al such that methoxy groups populate both the interior and external surface regions ($MFI_{slab}-CH_3^{int,surf}$) or only the interior region ($MFI_{slab}-CH_3^{int}$) of MFI's straight channels (Methods), as well as a purely siliceous material (MFI_{slab}). The free energy calculations revealed that only the former material exhibited a barrier to permeation across the surface ($q \approx -1.2$ nm; Fig. 7f). The height of the barrier in this case was comparable to those associated with internal diffusion. By contrast, the surface permeation in the other two materials ($MFI_{slab}-CH_3^{int}$ and MFI_{slab}) was essentially barrierless (Fig. 7f). Hence, consistent with the experimental observations, the free energy calculations collectively suggest that both internal mass transport and surface permeation are enhanced in Si-rich regions.

Conclusions

In this study, we identified a direct method to synthesize silicon-zoned ZSM-5 utilizing dual inorganic and organic SDAs. The siliceous exterior rim of Si-zoned ZSM-5 introduces surface passivation, which we showed is an effective approach to manipulate the mass transport properties of zeolite catalysts and reduce the accumulation of coke on external surfaces. The enhanced performance of Si-zoned catalysts relative to that of homogeneous counterparts suggests that diffusion limitations at the pore mouth of MFI-type materials are more pronounced for ZSM-5 compared those of silicalite-1. To this end, the synthesis approach presented here is an alternative to conventional methods aimed to reduce the size of the zeolite crystals. Here, we show for a series of MFI zeolites prepared with similar physicochemical properties, albeit different crystal sizes, that the comparatively larger Si-zoned samples behaved like much smaller particles with a markedly improved catalyst lifetime. Given the challenges of synthesizing ultrasmall (<100 nm) hierarchical zeolites, one-pot methods to generate zeolites with elemental zoning is an alternative and facile method to improve the diffusion properties of nanoporous catalysts.

Methods

Synthesis and catalyst preparation of ZSM-5 zeolites

A method based on organic structure-directing agents was used to synthesize Al-zoned ZSM-5 zeolites from a growth solution with a molar composition of 24TPAOH:100SiO_2:1.25Al_2O_3:0.4Na_2O:xNaCl(KCl):1,920H_2O:400EtOH, where x was varied between 0 and 12. NaOH, NaCl/KCl (if necessary) and TPAOH were mixed with deionized water followed by the addition of the silica source, colloidal silica (SM-30). EtOH was added to the mixture before the aluminium source, AIP (aluminum isopropoxide), was introduced. The mixtures were aged at room temperature for 24 h under continuous stirring. The growth solutions were then placed in a Teflon-lined stainless steel acid digestion bomb (Parr Instruments) and heated at 100 °C under autogenous pressure for 72 h.

The synthesis of ZSM-5 zeolites in a medium of fixed total SDA content (Na^+ and TPA^+) was performed using a growth solution with a molar composition of xTPAOH:100SiO_2:1.67Al_2O_3:(32 − x)NaOH:4,570H_2O (where x = 0–28.8). Using the same method, the ZSM-5 zeolites with a fixed total inorganic SDA content (Na^+ and/or K^+) were synthesized from a growth solution with a molar composition of xTPAOH:100SiO_2:1.67Al_2O_3:(32 − x)NaOH:xNaCl or KCl:4,570H_2O (where x = 7.4–28.8). The reagents NaOH, TPAOH, NaCl and KCl, and the aluminium source ($NaAlO_2$) were mixed with deionized water followed by the addition of the silica source (colloidal silica SM-30). The mixtures were aged at room temperature for 1 h under continuous stirring. The growth solutions were then placed in a Teflon-lined stainless-steel acid digestion bomb (Parr Instruments) and heated at 190 °C under autogenous pressure for 24 h.

The crystals were washed three times via centrifugation, dried at 50 °C in an oven and then calcined in flowing dried air (100 ml min^{-1}; Matheson Tri-Gas) for 5 h at 550 °C (heating rate of 1 °C min^{-1}). Ion exchange was performed using a 1 M NH_4NO_3 solution (2 wt% of calcined samples in the solutions) at 80 °C under continuous stirring for 2 h and three cycles. The ion-exchanged samples were dried and calcined by the aforementioned procedure to obtain H-form zeolites.

Time-elapsed study of the synthesis

To examine the crystallization process, we followed the previously outlined synthesis procedure and divided one synthesis solution into four different autoclaves. The autoclaves were placed in an oven at a set temperature and removed and quenched at periodic times (about 3, 6, 12 and 24 h). The supernatant was separated from the solids by centrifugation and diluted with a recorded dilution factor prior to the elemental analysis by inductively coupled plasma mass spectroscopy.

Characterization of ZSM-5 zeolites

Please refer to the Supplementary Methods for details on the zeolite characterization.

Reaction testing

The MTH reaction was carried out in a 6.35 mm stainless steel tube installed in a VTS clamshell furnace equipped with a Watlow controller. All the catalysts (40–60 mesh size) were diluted with silica gel (Davisol Grad 636; 35–60 mesh size) and held between two plugs of quartz wool. A K-type thermocouple (Omega Engineering) was inserted into the stainless steel tube to measure the temperature of the bottom of the catalyst bed. Prior to the reaction, the catalyst bed was pretreated in situ at 550 °C for 3 h under a flow of dried air (6 cm^3 min^{-1} of O_2 and 24 cm^3 min^{-1} of N_2; Matheson). The catalyst bed was then cooled to the reaction temperature, 350 °C. Methanol was fed by a syringe pump (Harvard Apparatus) into a heated inert gas stream of Ar (30 cm^3 min^{-1}; Matheson) to achieve a methanol partial pressure of 11.5 kPa. The molar space velocity was varied in the range 0.14–0.29 s^{-1} for the set of homogeneous and zoned samples. The first gas sampling was collected after a 20 min induction period. The reaction effluent was evaluated using an on-stream gas chromatograph (Agilent 7890B) equipped with a flame ionization detector and an Agilent DB-1 capillary column. Methanol and DME were considered as the reactants with the conversion X defined as:

$$X = [1 - C_{eff}/C_{feed}] \times 100\%, \quad (1)$$

where C_{eff} is the concentration of both methanol and DME in the effluent and C_{feed} is the concentration of methanol in the feed. The selectivity S_i of hydrocarbon product i is defined as:

$$S_i = [C_i/C_{t,eff}] \times 100\%, \quad (2)$$

where C_i is the concentration of hydrocarbon i in the effluent and $C_{t,eff}$ is the total concentration of hydrocarbons in the effluent. The TON was calculated using a previously reported equation[46]:

$$\mathrm{TON}(t) = \frac{1}{N_{H+}} \int_{t_1}^{t_2} F(\tau) \mathrm{d}\tau, \quad (3)$$

where N_{H+} is the total number of Brønsted acid sites (from NH_3–TPD and pyridine FTIR data), $F(\tau)$ is the molar flow rate of converted carbon (methanol and DME) and t is the time on stream. The integral applied to a discrete time interval (t_1 to t_2) yielded a discrete TON within the cumulative TON (Fig. 3d). Integrating with a larger time interval (from the starting point to a time at which all the catalysts reached a conversion of ~25%) yielded the total TON listed in Fig. 4a and Supplementary Table 5.

Characterization of catalysts postreaction

The coke content of the spent catalyst was determined by thermogravimetric analysis using a PerkinElmer STA 6000. In a typical experiment,

approximately 50 mg of spent catalyst was loaded into the apparatus and heated to 700 °C under a 20 ml min^{-1} airflow at a ramp rate of 10 °C min^{-1}. The coke content was quantified against the weight of dry zeolites after subtracting the moisture. The temperature ranges used to calculate the fractions of moisture and coke were 30–170 °C and 170–650 °C, respectively.

Operando UV–vis DR spectroscopy with gas chromatography

Operando UV–vis DR spectroscopy was used to track the evolution of the HP and coke species under methanol to olefin reaction conditions[57]. MTH reactions were performed in a fixed-bed quartz reactor. Similarly to the catalytic testing, the same amount of pelletized catalysts (212–425 µm) and silica gel were used for the operando UV–vis DR study. The mixture was heated to 550 °C for 3 h for activation with a flow of 100% oxygen, followed by cooling to 350 °C for the reaction. A 9 g g^{-1} h^{-1} weight hourly space velocity of methanol was used by flowing He gas through a methanol saturator (~20 °C). Meanwhile, the spectra in the range 200–1,000 nm were measured through a high-temperature UV–vis optical fibre (Avantes, 400 µm × 1.5 m, protected by a stainless steel sleeve) connected to an AvaSpec 2048L spectrometer using the reflection mode. During the measurements, the spectra were collected with an interval time of 30 s. The exposure time was ~50 ms, which then accumulated for 100 times.

Molecular dynamics simulations

USMD simulations were performed using LAMMPS (large-scale atomic/molecular massively parallel simulator software package, version 12 December 2018, https://www.lammps.org/)[69] along with the PLUMED 2.4.3 (ref. [70]) free energy plug-in (https://www.plumed.org/) to study molecular transport through the straight channels of the zeolite frameworks. The zeolite framework, acid sites and guest species (methanol and benzene) were modelled using the ReaxFF force field of Bai et al.[71], which can describe MFI materials substituted with aluminium sites occupied by Brønsted acids as well as methoxy groups; the latter are predicted to be prevalent under the conditions of MTH[72]. Internal transport through MFI's straight channel was investigated using a periodic 1 × 1 × 2 (2.01 × 1.97 × 2.63 nm^3) supercell of MFI that contained 192 T-sites that was generated from the crystallographic data (atomic positions and lattice parameters)[73]. Acidic versions of MFI were created by substituting the eight Si atoms located at the T8 sites in the straight channels of the framework with Al, which resulted in models with Si/Al ratios of 184/8 = 23. Coordination of the oxygens (O17) between the T8 and T7 sites was completed by adding either $-CH_3$ or –H to create MFI–CH_3 (methoxylated) and MFI–H (Brønsted acid) models, respectively. These choices were motivated by the density functional theory calculations of Ghorbanpour et al.[61], which showed that these acid substitutions were stable in the straight channel of MFI. Low loading conditions in each zeolite structure were investigated by computing the free energy profile for a single guest species initially inserted at the intersection of the straight and sinusoidal channels. For high methanol loading conditions expected under the MTH reaction conditions, 32 methanol molecules were inserted to achieve a loading of 16 molecules per unit cell; the free energy profile was computed for an additional methanol molecule initially inserted at the intersection of the straight and sinusoidal channels.

The atomic coordinates of the zeolite systems were refined using steepest descent energy minimization with a convergence criterion of 10^{-7} kcal mol^{-1}. A second round of energy minimization was then conducted in which the x, y and z dimensions of the simulation cell were allowed to relax independently under an applied stress of 1 atm. Three successive stages of molecular dynamics simulations were then performed to equilibrate the systems: 1 ns of simulation in the microcanonical ensemble, 1 ns in the canonical ensemble at 623 K and finally 3 ns in the isothermal–isostress ensemble at 623 K and 1 atm. The equations of motion were integrated using the velocity Verlet algorithm with a 0.5 fs time step. Temperature was maintained using a Langevin thermostat with a 0.1 ps damping constant. Isostress conditions were imposed using the Parrinello-Rahman[74] algorithm with a 0.2 ps time constant, which allowed the x, y and z dimensions of the simulation cell to fluctuate independently.

The quasi-2D slab models used to study surface permeation were generated from a 1 × 3 × 2 supercell of MFI by cleaving along the (010) plane at locations that minimize the number of broken Si–O bonds. The simulation cell was then extended in the normal direction to expose two identical (010) surfaces to a vacuum, and undercoordinated oxygens were protonated to create fully hydroxylated surfaces. The principal [010] axis of the generated slab was aligned along the y axis of the simulation cell. Two acidic slab systems were considered: one in which the Al substitutions and $-CH_3$ additions were made at the eight sites (T8 and O17 locations, respectively) located in the internal region of the slab and four located near the exposed surface ($MFI_{slab}-CH_3^{int,surf}$) and one in which only the eight internal sites were Al substituted ($MFI_{slab}-CH_3^{int}$). Permeation across a purely siliceous slab (MFI_{slab}) was also examined for comparison. The slab systems were energy minimized and then simulated, as described above, at a high methanol loading (16 molecules per unit cell). During energy minimization and simulations of the slab systems in the isothermal–isostress ensemble, only the x and z dimensions of the simulation cell (that is, those parallel to the (010) plane) were allowed to fluctuate, whereas the y dimension normal to the surface was held constant.

Following equilibration, USMD simulations were performed in the isothermal–isostress ensemble at 623 K and 1 atm to compute the potential of the mean force (free energy) as a function of the order parameter q, which characterizes the position of a selected guest molecule along the major axis of the straight channel. The order parameter q was defined as the y component of the distance between the guest species (methanol's carbon atom or benzene's centre of mass) and the centre of mass of the atoms that composed a selected ten-member ring in the straight channel of the zeolite framework. Independent 9-ns-long USMD simulations were performed in 6–34 adjacent windows evenly spaced along q, using a harmonic potential with spring constant K_{sp} = (750, 2000) kJ mol^{-1} nm^{-2} to restrain each simulation to its targeted region. Two auxiliary restraints were also applied during the USMD simulations. To prevent methanol and benzene from exploring the sinusoidal channels, an upper parabolic wall with force constant K_{sp} = (5000, 7500) kJ mol^{-1} nm^{-2} was applied for $r \geq 0.5$ nm, where r is the radial distance from the ten-member ring's centre of mass, defined analogously to q for the two species. A lower parabolic wall with K_{sp} = 1000 kJ mol^{-1} nm^{-2} was also applied on the global coordination number[75] CN ≤ 7.8 for the 8 acid groups in MFI–CH_3, MFI–H and $MFI_{slab}-CH_3^{int}$ and for CN ≤ 11.8 for the 12 acid groups in $MFI_{slab}-CH_3^{int,surf}$ to prevent them from hopping to other sites and undergoing rare reactions. The CN order parameter was evaluated with a 6–12 switching function:

$$\mathrm{CN} = \sum_{i=1}^{n}\sum_{j=1}^{n}\left(\frac{1-\left(\frac{r_{ij}-d_0}{r_0}\right)^6}{1-\left(\frac{r_{ij}-d_0}{r_0}\right)^{12}}\right), \quad (4)$$

where n is the number of acid groups, r_{ij} is the distance between O17 site i and acid species j (j is C or H for the methoxy or Brønsted acid groups, respectively), r_0 = 0.15 nm is the characteristic bonding distance and d_0 = 0.1 nm is the cutoff, which was chosen to ensure that pairs with r_{ij} of up to r_0 contribute 1 to the coordination. Estimates of the free energy profiles $F(q)$ were obtained by analysing the USMD trajectories using BayesWHAM[76], discarding data from the first 2 ns for equilibration and from frames in which the auxiliary restraints were nonzero.

Diffusivities for the guest species in the MFI frameworks were estimated from the $F(q)$ profiles using TST. According to TST, when

state i in the region $q \in (q_{il}, q_{ih})$ and state j in the region $q \in (q_{jl}, q_{jh})$, where subscripts l and h denote the lower and higher bounds of the interval, respectively, are separated by a high free energy maximum in $F(q)$ at the transition state $q = q^{\ddagger}$, the rate constant $k_{i\to j}^{\mathrm{TST}}$ associated with transitions from i to j is given by:

$$k_{i\to j}^{\mathrm{TST}} = \frac{1}{2}\langle|\dot{q}|\rangle_{\ddagger}\left(\frac{e^{-\frac{F(q^{\ddagger})}{k_{\mathrm{B}}T}}}{\int_{q_{il}}^{q_{ih}} e^{-\frac{F(q)}{k_{\mathrm{B}}T}}\,\mathrm{d}q}\right), \tag{5}$$

where T is the temperature and $\langle|\dot{q}|\rangle_{\ddagger}$ is the average absolute velocity along the reaction coordinate at the transition state[62,64]. Appropriate bounds for the stable states i to j and the transition regions were identified using the minima and maxima in $F(q)$ (Supplementary Table 8). Finally, the diffusivities were estimated using $D_{\mathrm{TST}}^{1\mathrm{D}} = \frac{1}{2}\lambda^2 k_{i\to j}^{\mathrm{TST}}$ (ref. [63]), where λ is the distance between neighbouring cages along the order parameter q and is estimated from the positions of the global free energy minima in $F(q)$.

The diffusivities evaluated using TST enabled a comparison of the dynamics of the guest species in the different MFI models (Supplementary Table 9), but an additional dynamical correction must be computed to obtain precise estimates. We evaluated the dynamical correction for methanol in several of the models using the effective positive flux (EPF) method[64]. The EPF calculations for each system were performed using 1000 independent microcanonical (NVE) molecular dynamics trajectories initiated from independent configurations extracted from an umbrella sampling window near the free energy maxima in (q) at $q \approx q^{\ddagger}$, using initial velocities from the Maxwell–Boltzmann distribution at 623 K. The molecular dynamics trajectories were propagated forwards and backwards in time until they reached a basin at the free energy minima in $F(q)$, defined as $q_{\mathrm{basin}} \in (q_{\mathrm{min}} - 0.08, q_{\mathrm{min}} + 0.08\ \mathrm{nm})$, saving the instantaneous value of q and the velocity along the reaction coordinate $\dot{q}$ at every time step. The transmission coefficient κ was computed from the trajectory ensemble as described in Peters[64], defining crossing points as configurations with $q \in (q^{\ddagger} - 0.0005, q^{\ddagger} + 0.0005\ \mathrm{nm})$. Finally, the dynamically corrected TST (cTST) diffusivity was estimated[65] using:

$$D_{\mathrm{cTST}}^{1\mathrm{D}} = \kappa D_{\mathrm{TST}}^{1\mathrm{D}}. \tag{6}$$

The steered molecular dynamics simulations used to generate Supplementary Videos 1–4 were performed in the NσT ensemble at 623 K and 1 atm. A moving harmonic restraint with a spring constant of 500 kJ mol^{-1} nm^{-2} was applied along the order parameter q to pull each guest species through the straight channels of the MFI frameworks at an average velocity of 0.13 nm ns^{-1}. The same auxiliary restraints described above were also applied during the steered molecular dynamics simulations.

Data availability

Source data are provided with this paper. Data of main and extended data figures are available in the Supplementary Information, an online repository and upon request. Data from the molecular simulation studies are available in the online repository, including figure data, data from the USMD simulations (example input scripts for LAMMPS 12 December 2018 and PLUMED 2.4.3, initial and final configurations from the trajectories and BayesWHAM analysis scripts), and scripts and input files for evaluating the transmission coefficients using the effective positive flux method. Correspondence and request for materials should be addressed to J.D.R. or B.M.W.

References

1. Choi, M. et al. Stable single-unit-cell nanosheets of zeolite MFI as active and long-lived catalysts. *Nature* **461**, 246–249 (2009).
2. Zhang, X. et al. Synthesis of self-pillared zeolite nanosheets by repetitive branching. *Science* **336**, 1684–1687 (2012).
3. Fan, W. et al. Hierarchical nanofabrication of microporous crystals with ordered mesoporosity. *Nat. Mater.* **7**, 984–991 (2008).
4. Lupulescu, A. I., Kumar, M. & Rimer, J. D. A facile strategy to design zeolite L crystals with tunable morphology and surface architecture. *J. Am. Chem. Soc.* **135**, 6608–6617 (2013).
5. Chaikittisilp, W. et al. Formation of hierarchically organized zeolites by sequential intergrowth. *Angew. Chem. Int. Ed.* **52**, 3355–3359 (2013).
6. Awala, H. et al. Template-free nanosized faujasite-type zeolites. *Nat. Mater.* **14**, 447–451 (2015).
7. Sachse, A. et al. Development of intracrystalline mesoporosity in zeolites through surfactant templating. *Cryst. Growth Des.* **17**, 4289–4305 (2017).
8. Willhammar, T. et al. Structure and catalytic properties of the most complex intergrown zeolite ITQ-39 determined by electron crystallography. *Nat. Chem.* **4**, 188–194 (2012).
9. Na, K. et al. Pillared MFI zeolite nanosheets of a single-unit-cell thickness. *J. Am. Chem. Soc.* **132**, 4169–4177 (2010).
10. Dai, H. et al. Finned zeolite catalysts. *Nat. Mater.* **19**, 1074–1080 (2020).
11. Schmidt, J. E. et al. Coke formation in a zeolite crystal during the methanol-to-hydrocarbons reaction as studied with atom probe tomography. *Angew. Chem. Int. Ed.* **55**, 11173–11177 (2016).
12. Kunieda, T., Kim, J. H. & Niwa, M. Source of selectivity of *p*-xylene formation in the toluene disproportionation over HZSM-5 zeolites. *J. Catal.* **188**, 431–433 (1999).
13. Qin, W., Zhou, Y. & Rimer, J. D. Deleterious effects of non-framework Al species on the catalytic performance of ZSM-5 crystals synthesized at low temperature. *React. Chem. Eng.* **4**, 1957–1968 (2019).
14. Wang, C. et al. Maximizing sinusoidal channels of HZSM-5 for high shape-selectivity to *p*-xylene. *Nat. Commun.* **10**, 4348 (2019).
15. Aramburo, L. R. et al. The porosity, acidity, and reactivity of dealuminated zeolite ZSM-5 at the single particle level: the influence of the zeolite architecture. *Chem. Eur. J.* **17**, 13773–13781 (2011).
16. Kim, K., Ryoo, R., Jang, H.-D. & Choi, M. Spatial distribution, strength, and dealumination behavior of acid sites in nanocrystalline MFI zeolites and their catalytic consequences. *J. Catal.* **288**, 115–123 (2012).
17. Yang, D.J. Process for coating crystalline silica polymorphs. European Patent 4452909 (1982).
18. Rodewald, P.G. Silica-modified zeolite catalysts. US patent 4402867A (1981).
19. Von Ballmoos, R. & Meier, W. M. Zoned aluminium distribution in synthetic zeolite ZSM-5. *Nature* **289**, 782–783 (1981).
20. Althoff, R., Schulz-Dobrick, B., Schüth, F. & Unger, K. Controlling the spatial distribution of aluminum in ZSM-5 crystals. *Micropor. Mater.* **1**, 207–218 (1993).
21. Groen, J. C. et al. Creation of hollow zeolite architectures by controlled desilication of Al-zoned ZSM-5 crystals. *J. Am. Chem. Soc.* **127**, 10792–10793 (2005).
22. Danilina, N., Krumeich, F., Castelanelli, S. A. & van Bokhoven, J. A. Where are the active sites in zeolites? Origin of aluminum zoning in ZSM-5. *J. Phys. Chem. C.* **114**, 6640–6645 (2010).
23. Ristanović, Z. et al. Intergrowth structure and aluminium zoning of a zeolite ZSM-5 crystal as resolved by synchrotron-based micro X-ray diffraction imaging. *Angew. Chem. Int. Ed.* **52**, 13382–13386 (2013).
24. Kim, J. H., Ishida, A., Okajima, M. & Niwa, M. Modification of HZSM-5 by CVD of various silicon compounds and generation of *para*-selectivity. *J. Catal.* **161**, 387–392 (1996).

25. Zheng, S., Heydenrych, H. R., Jentys, A. & Lercher, J. A. Influence of surface modification on the acid site distribution of HZSM-5. *J. Phys. Chem. B* **106**, 9552–9558 (2002).
26. Jae, J. et al. Investigation into the shape selectivity of zeolite catalysts for biomass conversion. *J. Catal.* **279**, 257–268 (2011).
27. Ennaert, T. et al. Potential and challenges of zeolite chemistry in the catalytic conversion of biomass. *Chem. Soc. Rev.* **45**, 584–611 (2016).
28. Zheng, S., Heydenrych, H. R., Röger, H. P., Jentys, A. & Lercher, J. A. On the enhanced selectivity of HZSM-5 modified by chemical liquid deposition. *Top. Catal.* **22**, 101–106 (2003).
29. Cheng, Y.-T., Zhuopeng, W., Gilbert, C. J., Wei, F. & Huber, G. W. Production of *p*-xylene from biomass by catalytic fast pyrolysis using ZSM-5 catalysts with reduced pore openings. *Angew. Chem. Int. Ed.* **51**, 11097–11100 (2012).
30. Foster, A. J., Jae, J., Cheng, Y.-T., Huber, G. W. & Lobo, R. F. Optimizing the aromatic yield and distribution from catalytic fast pyrolysis of biomass over ZSM-5. *Appl. Catal. A* **423–424**, 154–161 (2012).
31. Yan, Z. et al. On the acid-dealumination of USY zeolite: a solid state NMR investigation. *J. Mol. Catal. A* **194**, 153–167 (2003).
32. Le, T. T., Chawla, A., & Rimer, J. D. Impact of acid site speciation and spatial gradients on zeolite catalysis. *J. Catal.* **391**, 56–68 (2020).
33. Knott, B. C. et al. Consideration of the aluminum distribution in zeolites in theoretical and experimental catalysis research. *ACS Catal.* **8**, 770–784 (2017).
34. Ravi, M., Sushkevich, V. L. & van Bokhoven, J. A. Towards a better understanding of Lewis acidic aluminium in zeolites. *Nat. Mater.* **19**, 1047–1056 (2020).
35. Persson, A. E., Schoeman, B. J., Sterte, J. & Ottesstedt, J. E. The synthesis of discrete colloidal particles of TPA–silicalite-1. *Zeolites* **14**, 557–567 (1994).
36. Dai, F. Y., Suzuki, M., Takahashi, H. & Saito, I. Mechanism of zeolite crystallization without using template reagents of organic bases. *Stud. Surf. Sci. Catal.* **28**, 223–230 (1986).
37. Chawla, A. et al. Cooperative effects of inorganic and organic structure-directing agents in ZSM-5 crystallization. *Mol. Syst. Des. Eng.* **3**, 159–170 (2018).
38. Meng, L. et al. A dual-templating synthesis strategy to hierarchical ZSM-5 zeolites as efficient catalysts for the methanol-to-hydrocarbons reaction. *J. Catal.* **361**, 135–142 (2018).
39. Mores, D. et al. Core–shell H-ZSM-5/silicalite-1 composites: Brønsted acidity and catalyst deactivation at the individual particle level. *Phys. Chem. Chem. Phys.* **13**, 15985–15994 (2011).
40. Karwacki, L. et al. Morphology-dependent zeolite intergrowth structures leading to distinct internal and outer-surface molecular diffusion barriers. *Nat. Mater.* **8**, 959–965 (2009).
41. Vonballmoos, R. & Meier, W. M. Zoned aluminum distribution in synthetic zeolite ZSM-5. *Nature* **289**, 782–783 (1981).
42. Li, T., Krumeich, F., Chen, M., Ma, Z. & van Bokhoven, J. A. Defining aluminum zoning during synthesis of ZSM-5 zeolites. *Phys. Chem. Chem. Phys.* **734**, 734–739 (2020).
43. Li, T. et al. Variation of aluminium distribution in small-sized ZSM-5 crystals during desilication. *Chem. Eur. J.* **25**, 15879–15886 (2019).
44. Li, T., Krumeich, F. & van Bokhoven, J. A. Where does the zeolite ZSM-5 nucleation and growth start? The effect of aluminum. *Cryst. Growth Des.* **19**, 2548–2551 (2019).
45. Shen, Y. et al. Deconvoluting the competing effects of zeolite framework topology and diffusion path length on methanol to hydrocarbons reaction. *ACS Catal.* **8**, 11042–11053 (2018).
46. Khare, R., Millar, D. & Bhan, A. A mechanistic basis for the effects of crystallite size on light olefin selectivity in methanol-to-hydrocarbons conversion on MFI. *J. Catal.* **321**, 23–31 (2015).
47. Cavalcante, C. L. Jr & Ruthven, D. M. Adsorption of branched and cyclic paraffins in silicalite. 2. Kinetics. *Ind. Eng. Chem. Res.* **34**, 185–191 (1995).
48. Gao, M. B. et al. Direct quantification of surface barriers for mass transfer in nanoporous crystalline materials. *Commun. Chem.* **2**, 43–52 (2019).
49. Khare, R., Liu, Z. H., Han, Y. & Bhan, A. A mechanistic basis for the effect of aluminum content on ethene selectivity in methanol-to-hydrocarbons conversion on HZSM-5. *J. Catal.* **348**, 300–305 (2017).
50. Olsbye, U. et al. The formation and degradation of active species during methanol conversion over protonated zeotype catalysts. *Chem. Soc. Rev.* **44**, 7155–7176 (2015).
51. Yarulina, I., Chowdhury, A. D., Meirer, F., Weckhuysen, B. W. & Gascon, J. Recent trends and fundamental insights in the methanol-to-hydrocarbons process. *Nat. Catal.* **1**, 398–411 (2018).
52. Remi, J. C. S. et al. The role of crystal diversity in understanding mass transfer in nanoporous materials. *Nat. Mater.* **15**, 401–406 (2016).
53. Hwang, A. et al. Effects of diffusional constraints on lifetime and selectivity in methanol-to-olefins catalysis on HSAPO-34. *J. Catal.* **369**, 122–132 (2018).
54. Yarulina, I. et al. Structure–performance descriptors and the role of Lewis acidity in the methanol-to-propylene process. *Nat. Chem.* **10**, 804–812 (2018).
55. Fu, D., van der Heijden, O., Stanciakova, K., Schmidt, J. E. & Weckhuysen, B. M. Disentangling reaction processes of zeolites within single-oriented channels. *Angew. Chem. Int. Ed.* **59**, 15502–15506 (2020).
56. Goetze, J. et al. Insights into the activity and deactivation of the methanol-to-olefins process over different small-pore zeolites as studied with operando UV–vis spectroscopy. *ACS Catal.* **7**, 4033–4046 (2017).
57. Borodina, E. et al. Influence of the reaction temperature on the nature of the active and deactivating species during methanol to olefins conversion over H-SSZ-13. *ACS Catal.* **5**, 992–1003 (2015).
58. Barbera, K., Bonino, F., Bordiga, S., Janssens, T. V. W. & Beato, P. Structure–deactivation relationship for ZSM-5 catalysts governed by framework defects. *J. Catal.* **280**, 196–205 (2011).
59. Qin, Z. et al. Comparative study of nano-ZSM-5 catalysts synthesized in OH^- and F^- media. *Adv. Func. Mater.* **24**, 257–264 (2014).
60. Paul, G. et al. Combined solid-state NMR, FT-IR and computational studies on layered and porous materials. *Chem. Soc. Rev.* **47**, 5684–5739 (2018).
61. Ghorbanpour, A., Rimer, J. D. & Grabow, L. C. Periodic, vdW-corrected density functional theory investigation of the effect of Al siting in H-ZSM-5 on chemisorption properties and site-specific acidity. *Catal. Commun.* **52**, 98–102 (2014).
62. Smit, B. & Maesen, T. L. M. Molecular simulations of zeolites: adsorption, diffusion, and shape selectivity. *Chem. Rev.* **108**, 4125–4184 (2008).
63. Kolokathis, P. D., Kali, G., Jobic, H. & Theodorou, D. N. Diffusion of aromatics in silicalite-1: experimental and theoretical evidence of entropic barriers. *J. Phys. Chem. C.* **120**, 21410–21426 (2016).
64. Peters, B. *Reaction Rate Theory and Rare Events* (Elsevier, 2017).
65. Teixeira, A. R. et al. Dominance of surface barriers in molecular transport through silicalite-1. *J. Phys. Chem. C* **117**, 25545–25555 (2013).
66. Hibbe, F. et al. The nature of surface barriers on nanoporous solids explored by microimaging of transient guest distributions. *J. Am. Chem. Soc.* **133**, 2804–2807 (2011).
67. Sastre, G., Karger, J. & Ruthven, D. M. Surface barriers and symmetry of adsorption and desorption processes. *Adsorption* **27**, 777–785 (2021).

68. Wang, R. et al. Art of architecture: efficient transport through solvent-filled metal–organic frameworks regulated by topology. *Chem. Mater.* **33**, 6832–6840 (2021).
69. Plimpton, S. Fast parallel algorithms for short-range molecular dynamics. *J. Comput. Phys.* **117**, 1–19 (1995).
70. Tribello, G. A., Bonomi, M., Branduardi, D., Camilloni, C. & Bussi, G. PLUMED 2: new feathers for an old bird. *Comput. Phys. Commun.* **185**, 604–613 (2014).
71. Bai, C., Liu, L. & Sun, H. Molecular dynamics simulations of methanol to olefin reactions in HZSM-5 zeolite using a ReaxFF force field. *J. Phys. Chem. C* **116**, 7029–7039 (2012).
72. Nastase, S. A. F. et al. Mechanistic insight into the framework methylation of H-ZSM-5 for varying methanol loadings and Si/Al ratios using first-principles molecular dynamics simulations. *ACS Catal.* **10**, 8904–8915 (2020).
73. Database of Zeolite Structures (International Zeolite Association Structure Commission, accessed 2023); http://www.iza-structure.org/databases/
74. Parrinello, M. & Rahman, A. Polymorphic transitions in single crystals: a new molecular dynamics method. *J. Appl. Phys.* **52**, 7182–7190 (1981).
75. Zheng, S. & Pfaendtner, J. Enhanced sampling of chemical and biochemical reactions with metadynamics. *Mol. Simul.* **41**, 55–72 (2015).
76. Ferguson, A. L. BayesWHAM: a Bayesian approach for free energy estimation, reweighting, and uncertainty quantification in the weighted histogram analysis method. *J. Comput. Chem.* **38**, 1583–1605 (2017).

Acknowledgements

J.D.R. acknowledges support primarily from the US Department of Energy, Office of Science, Office of Basic Energy Sciences under Award no. DE-SC0014468. Additional support was provided by the Welch Foundation (Award E-1794 to J.D.R. and Award E-1882 to J.C.P.). This work is supported by the NWO Gravitation program, Netherlands Center for Multiscale Catalytic Energy Conversion (MCEC) and a European Research Council (ERC) Advanced Grant (no. 321140). This research used resources of the National Synchrotron Light Source II, a US Department of Energy (DOE) Office of Science User Facility operated for the DOE Office of Science by Brookhaven National Laboratory under contract no. DE-SC0012704. We thank J. E. Schmidt (Utrecht University) for useful discussions. We also thank A. Bhan (University of Minnesota) and Z. Shi (University of Minnesota) for their help with diffusivity measurements and technical guidance. M.E. Davis (Caltech) is acknowledged for assistance with TGA measurements. Computational resources were generously provided by the Hewlett Packard Enterprise Data Science Institute at the University of Houston and the Texas Advanced Computing Center at the University of Texas at Austin.

Author contributions

J.D.R., W.Q. and T.T.L. conceived the project and designed the experiments. T.T.L., W.Q., N.N., D.F. and M.D.P. were primarily responsible for the data collection and analysis. B.M.W. was responsible for the operando UV–vis DR measurements and also discussed the project concept and related experiments with J.D.R. and T.T.L. C.W. and S.R.B. were responsible for the VKE–XPS measurements and data analysis. J.D.R. was responsible for the zeolite synthesis, characterization and catalytic testing. J.C.P. and A.A. were responsible for the molecular dynamics simulations and discussions of the mechanistic interpretations. J.D.R. and T.T.L. wrote the manuscript and prepared the figures with help from the other coauthors. All the authors contributed to scientific discussions and the preparation as well as the revisions of the manuscript and Supplementary Information materials.

Competing interests

The authors declare no competing interests.

Additional information

Extended data is available for this paper at https://doi.org/10.1038/s41929-023-00927-2.

Supplementary information The online version contains supplementary material available at https://doi.org/10.1038/s41929-023-00927-2.

Correspondence and requests for materials should be addressed to Bert M. Weckhuysen or Jeffrey D. Rimer.

Peer review information *Nature Catalysis* thanks Svetlana Mintova and the other, anonymous, reviewers for their contribution to the peer review of this work.

https://doi.org/10.1038/s41929-023-00927-2

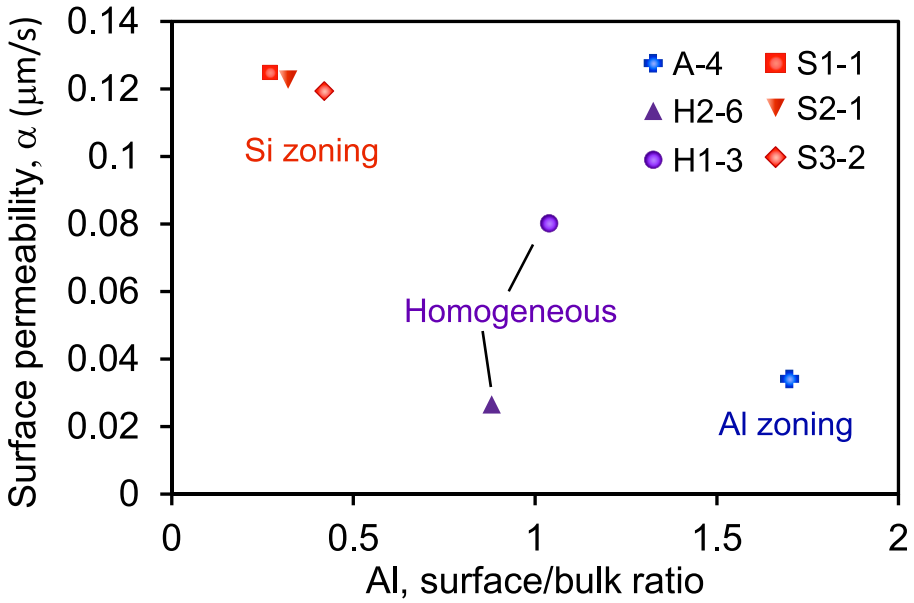

Extended Data Fig. 1 | Surface permeability of zoned and homogeneous zeolite samples. Surface permeability, α, from fitting early uptake data in Supplementary Fig. 9 with a spherical particle model, plotted against the Al surface-to-bulk ratio of the following samples: Si-zoned (red symbols), homogeneous (purple symbols), and Al-zoned (blue symbol) zeolites.

https://doi.org/10.1038/s41929-023-00927-2

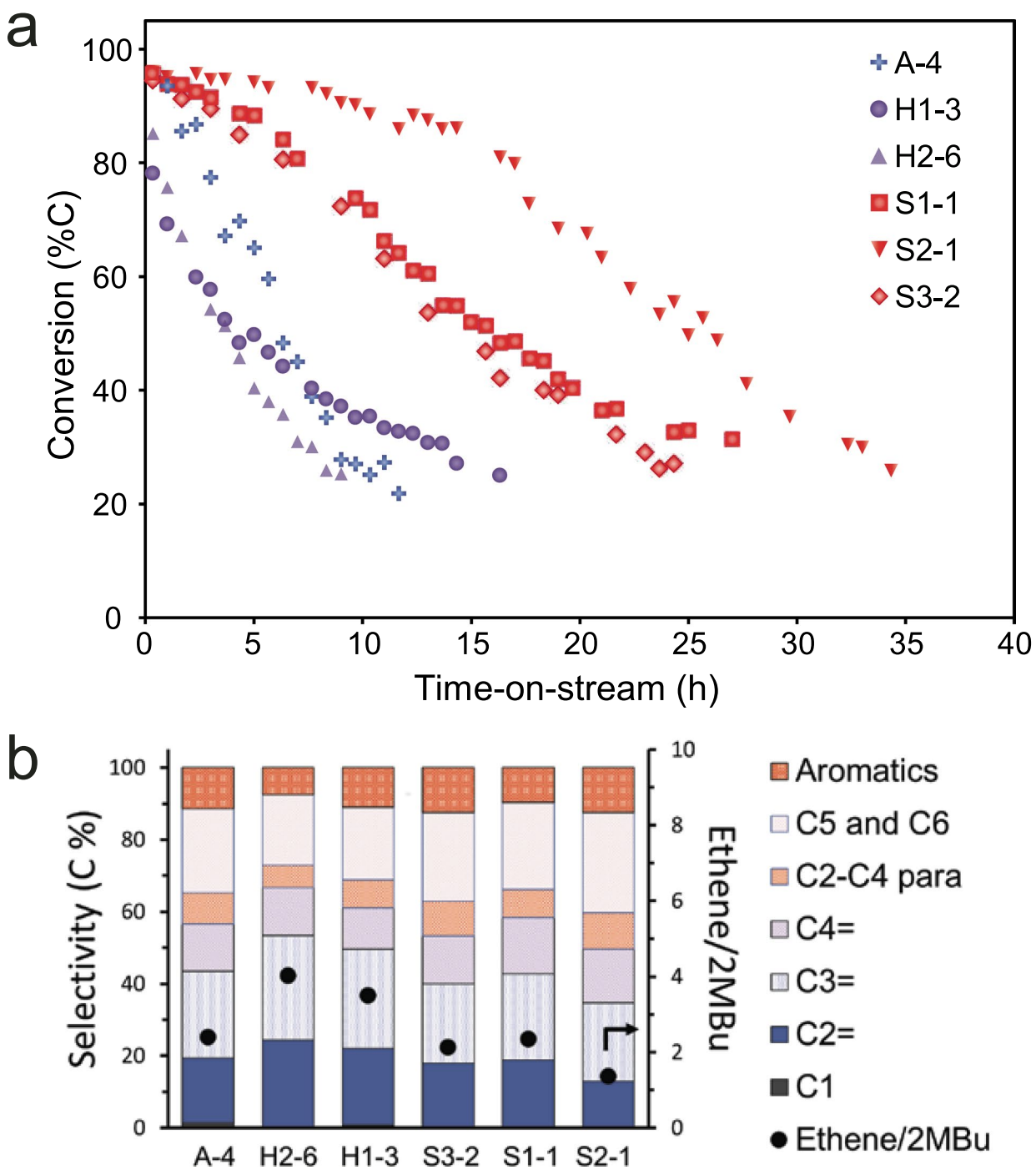

Extended Data Fig. 2 | Conversion and selectivity of zoned and homogeneous zeolite catalysts. a, Conversion of methanol and dimethyl ether as a function of time-on-stream for the Al-zoned sample A-4 (blue cross), homogeneous samples H1-3 (purple circles) and H2-6 (purple triangles), and Si-zoned samples S1-1 (red squares), S2-1 (red inverted triangles), and S3-2 (red diamonds). All reactions were performed at 350 °C using a space velocity of 0.18–0.30 mol MeOH mol^{-1} H^{+} s^{-1}. **b**, Selectivity profile (left y-axis) at sub-100% conversion (initial data point after 20 min induction period) and the ratio of ethene to the sum of 2-methylbutane and 2-methylbutene (symbols, right y-axis).

https://doi.org/10.1038/s41929-023-00927-2

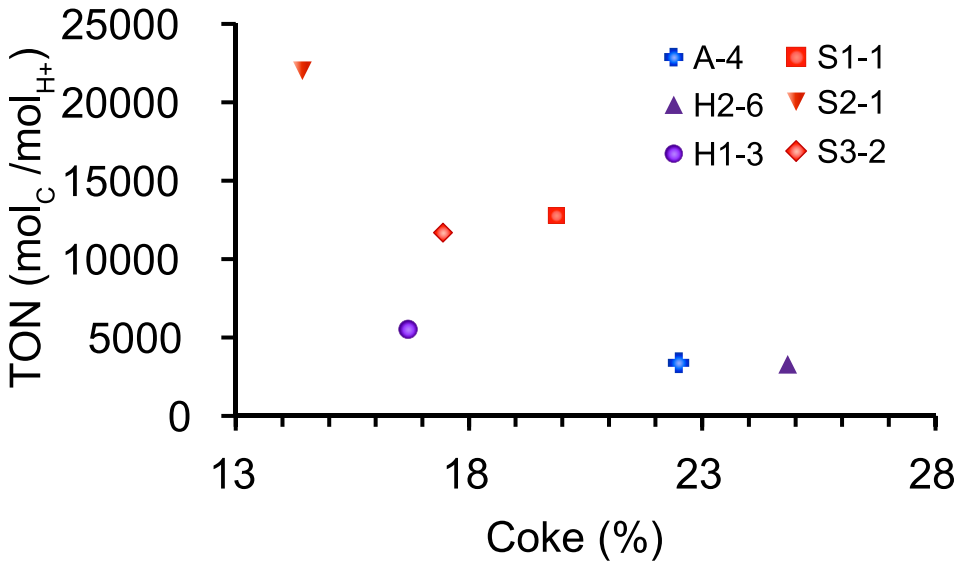

Extended Data Fig. 3 | Relationship between turnover number and coke accumulation in zoned and homogeneous zeolite catalysts. Turnover number (TON) of each tested catalyst plotted against the coke content in dry zeolite samples (listed in Supplementary Table 7).

https://doi.org/10.1038/s41929-023-00927-2

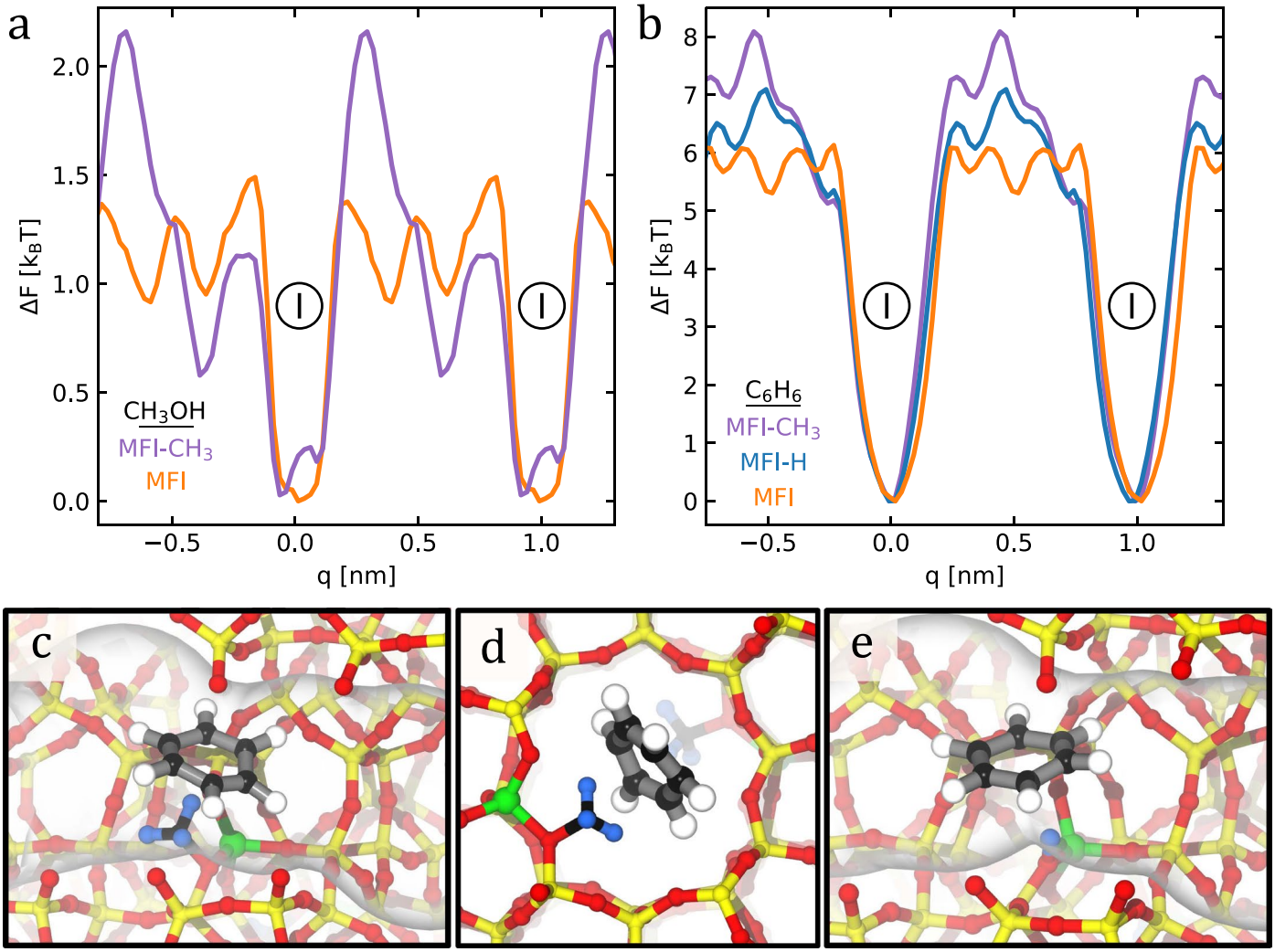

Extended Data Fig. 4 | Molecular dynamics simulations of methanol and benzene diffusion in zeolite MFI. a, Free energy profile at 350 °C (potential of mean force, in units of the thermal energy $k_BT \approx 0.0537$ *eV* at T = 350 °C) for internal diffusion of methanol in the high loading limit (that is, 16 methanol per unit cell) through the straight channel (b-direction) of MFI with: aluminium sites (Si/Al = 23) occupied by methoxy groups (purple, MFI-CH_3) and a purely siliceous material (orange, MFI). **b**, Free energy profile for internal diffusion of benzene in the low loading limit through the straight channel of MFI with: aluminum sites occupied by methoxy groups (purple, MFI-CH_3) and Brønsted acids (blue, MFI-H), and purely siliceous material (orange, MFI). **c**, **d**, Images of benzene from Supplementary Movie 3 diffusing through a straight channel populated with methoxy groups. **e**, Image of benzene from Supplementary Movie 4 diffusing through a straight channel with Brønsted acid sites. Atom coloring is as follows: Si (yellow), O (red), H on acidic groups (blue), Al (green), C (black), and H on guest species (white).